Doppler velocimeter and vibrometer FMCW LiDAR with Si photonic crystal beam scanner

SANEYUKI SUYAMA, HIROYUKI ITO, RYO KURAHASHI, HIROSHI ABE, AND TOSHIHIKO BABA[*] [ID]

Department of Electrical and Computer Engineering, Yokohama National University, 79-5 Tokiwadai, Hodogaya-ku, Yokohama 240-8501, Japan
[*]*baba-toshihiko-zm@ynu.ac.jp*

Abstract: In this paper, we propose and demonstrate a frequency-modulated continuous-wave light detection and ranging (LiDAR) with a Si photonic crystal beam scanner, simultaneously enabling scanning laser Doppler measurements. This nonmechanical solid-state device can reduce the size of conventional scanning laser Doppler vibrometers, making LiDAR a multimodal imaging sensor, which can measure the distributions of distance, velocity, and vibration frequency. We fabricated this device using Si photonics process and confirmed the expected operations. Distance and velocity resolutions were less than 15 mm and 19 mm/s, respectively. The detection limit of the vibration amplitude determined by the signal-to-noise ratio was 2.5 nm.

1. Introduction

Light detection and ranging (LiDAR) is a three-dimensional (3D) imaging sensor, applicable to self-driving vehicles, robotics, drones, mapping, and so on [1]. LiDAR is usually comprised of a laser source, beam scanner and photodiode. In recent years, optical phased array (OPA) [2–8], focal plane array (FPA) [9–11], and slow light grating (SLG) [12,13], which are fabricated by Si photonics technology, have been actively studied as compact and nonmechanical solid-state beam scanners. Additionally, integrated LiDAR incorporating many of these components on a single chip have been demonstrated [11]. We have also demonstrated wide-angle, high-resolution solid-state beam scanning using SLG based on photonic crystal waveguides (PCWs).

Time of flight (ToF), which measures the round-trip delay of an optical pulse, is commonly used as the ranging method in commercial LiDAR systems. When Si photonics, particularly with Si waveguides, is applied to LiDAR, two-photon absorption occurs even at telecom wavelengths and strongly constrains the pulse intensity and, thus, the LiDAR sensitivity. Consequently, many studies have employed the frequency-modulated continuous-wave (FMCW) method, which does not use an optical pulse, but FMCW light. The range information is obtained from the beat frequency between round-trip light and reference light via coherent homodyne detection. In principle, this method provides shot-noise-limit high sensitivity and high-range resolution determined by the frequency modulation bandwidth and does not interfere with ambient light and other LiDARs.

A more significant feature of the FMCW method is that the velocity of objects can also be obtained by detecting Doppler shifts [6,11,14]. If the range and velocity are acquired simultaneously in two dimensions (2D), it will be quite useful for exactly analyzing high-speed moving objects, such as self-driving vehicles and drones, to predict subsequent motions and, thus, increase their safety. Combining the principle of scanning laser Doppler vibrometer (SLDV) [15–17] with the FMCW, the vibration distribution of objects can also be visualized. SLDV is used to inspect vibrating equipment, infrastructure, and human health conditions [18,19]. Currently, its large size and expense limit its applications. If an on-chip FMCW LiDAR is realized by Si photonics, a multimodal imaging sensor will evolve, which will function as a

velocimeter and vibrometer beyond the capability of standard ToF LiDARs and acquire further applications.

In this study, we demonstrated the operation of such a multimodal LiDAR with an SLG beam scanner. In Section 2 of this paper, we briefly summarize the theory of the velocimeter and vibrometer combined with the FMCW LiDAR. Subsequent sections describe the setup of the experiment and then present the experimental results of each function, followed by the conclusions.

2. Theory

The FMCW LiDAR measures the frequency difference (beat frequency f_b) between reflected signal light and reference light and obtains the range R to the target object by the following equation [20]:

$$R = \frac{cT}{2B}f_b. \tag{1}$$

where c is the speed of light in the environment, T is the frequency sweep period, and B is the frequency sweep bandwidth, assuming linear frequency sweep as the frequency modulation. The range resolution ΔR is given from the sampling theorem, $\Delta f_b = 1/T$, and is expressed as

$$\Delta R = \frac{c}{2B}. \tag{2}$$

For example, $\Delta R = 15$ mm for $B = 10$ GHz.

When the target object has a velocity component v in the direction of light travel, f_b is Doppler-shifted by f_D, resulting in frequencies of $f_{up} = f_b + f_D$ and $f_{down} = f_b - f_D$ for a triangular frequency sweep. For the wavelength λ of light, v is given as

$$v = \frac{(f_{up} - f_{down})\lambda}{4} = \frac{f_D\lambda}{2}. \tag{3}$$

The velocity resolution Δv is given under the condition $f_b = f_D$, then

$$\Delta v = \frac{\lambda}{2T}. \tag{4}$$

For example, $\Delta v = 19$ mm/s for $T = 40$ μs and $\lambda = 1550$ nm.

When the target is displaced by $x(t)$ along the direction of light travel with respect to time t, the FMCW beat signal S is given as [21–23]

$$S \propto \cos^2[2\pi f_b t + \phi(t)], \quad \phi(t) = 2k_0 x(t) \tag{5}$$

where k_0 is the wavenumber in the environment. When the target is vibrating sinusoidally with the amplitude ΔX and frequency f_v, which is,

$$x(t) = \Delta X \sin(2\pi f_v t). \tag{6}$$

Equation (5) is expanded as

$$S \propto \left[\begin{array}{l} J_0\left(\frac{4\pi\Delta X}{\lambda}\right) - \sum_{k=1}^{n} J_{2k-1}\left(\frac{4\pi\Delta X}{\lambda}\right) \left[\begin{array}{l} \cos 2\pi\{f_b - (2k-1)f_v\}t \\ - \cos 2\pi\{f_b - (2k+1)f_v\}t \end{array} \right] \\ + \sum_{k=1}^{n} J_{2k}\left(\frac{4\pi\Delta X}{\lambda}\right) \{\cos 2\pi(f_b - 2kf_v)t + \cos 2\pi(f_b + 2kf_v)t\} \end{array} \right]^2 \tag{7}$$

This equation indicates that sidebands with integer multiple frequencies of f_v are generated around f_b. The spectral intensity ratio of $f_b + f_v$ to f_b is given as

$$S_1/S_0 = \left| J_1\left(\frac{4\pi\Delta X}{\lambda}\right) \middle/ J_0\left(\frac{4\pi\Delta X}{\lambda}\right) \right|^2. \tag{8}$$

For example, $\Delta X = 2.5$ nm for $S_1/S_2 = -40$ dB and $\lambda = 1550$ nm.

3. Setup

Figure 1 shows the measurement setup used. Output light from a bench-top tunable laser (Santec TSL-550) was modulated by LiNbO$_3$ in-phase/quadrature-phase modulator (IQ MOD, Thorlabs LN86-14-P-A-A). A frequency swept signal of 1–11 GHz ($B = 10$ GHz) generated by an arbitrary waveform generator (Keysight M9502A) was used for the modulation, which determined the range resolution $\Delta R = 15$ mm. Frequency-modulated light with a suppression ratio of 20 dB for unwanted frequency components was obtained. This was amplified by erbium-doped fiber amplifiers (EDFA, Thorlabs EDFA 100P, Alnair Labs HPA-200CL-30-PM-FA-FA) and a bandpass filter (Alnair Labs CNF220CL) and was split into signal and reference light at a ratio of 99:1. The signal light with polarization controlled to transverse electric was launched at the beam scanner chip. We have reported details of the chip in [24]. A 5-μm-wide channel waveguide was fabricated on a 210-nm-thick Si slab with a square array of perforated holes with a lattice constant $a = 380$ nm and a diameter $2r = 345$ nm, which we refer to as a bulk photonic crystal waveguide (BPCW). A shallow grating with a 10 nm depth, 300 nm width, and the period of $2a$ was formed on of the Si slab to emit the guided mode to the free space. The wavelength sweep was used to scan the emitted beam in the θ direction along the BPCW. To couple the light into the chip, we used a lensed fiber and an end-fire spot size converter. The emitted light was collimated by a cylindrical plano-convex lens of 50 mm focal length, because the emitted beam was fan-shaped and expanded in the direction across the BPCW (ϕ direction). Another plano-convex lens of 700 mm focal length was placed 300 mm from the BPCW to reduce the slight divergence in the θ direction. Reflected light from the object was received by the same BPCW through the reverse path of transmission, mixed with the reference light through the circulator, detected by an InGaAs balanced photodiode (Discovery Semiconductors DSC710-39-FC), and analyzed by a spectrum analyzer (Rohde & Schwarz, FSW 43). In this experiment, we used these external components, but it is possible to integrate all of these components except for the laser, EDFA, and spectrum analyzer by using Si photonics technology. Although we used a combination of the BPCW, wavelength sweep, and plano-convex lenses for convenience of the experiment, it is also possible to use a standard PCW with a built-in thermo-optic heater for faster beam scanning and a prism lens for wide-angle collimation.
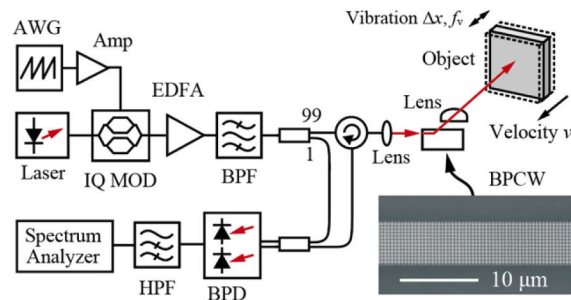

Fig. 1. Measurement setup and a confocal laser micrograph of BPCW for optical beam scanning, transmission, and reception.

4. Velocity measurement

The velocity was measured on the sidewall of a turntable (diameter $D = 330$ mm), as shown in Figs. 2(a) and 2(b). To enhance reflected light intensity toward the BPCW, a retroreflective sheet (ORALITE AP1000) was pasted on the sidewall. The distance from the BPCW to the sidewall, R, was approximately 4.08 m. The laser wavelength was swept in the range from 1535–1553 nm, and the beam was scanned in the range of $\theta \approx \pm 1.25°$. In the ϕ direction, the offset against the plano-convex lens tilted the beam, and thus 2D beam scanning was obtained. Figure 2(a) also shows the scanned beam shining on the sidewalls, which was observed by an InGaAs camera. When a triangular modulation with $T = 40$ μs was used for the frequency sweep, the beat spectrum was measured, as shown in Figs. 2(c) and 2(d). Without rotating the turntable, the beat spectrum appeared at 17.4 MHz, with a full width at half maximum (FWHM) of 20 Hz (determined by the resolution of the spectrum analyzer setting) and a signal-to-noise ratio (S/N) of 65 dB.
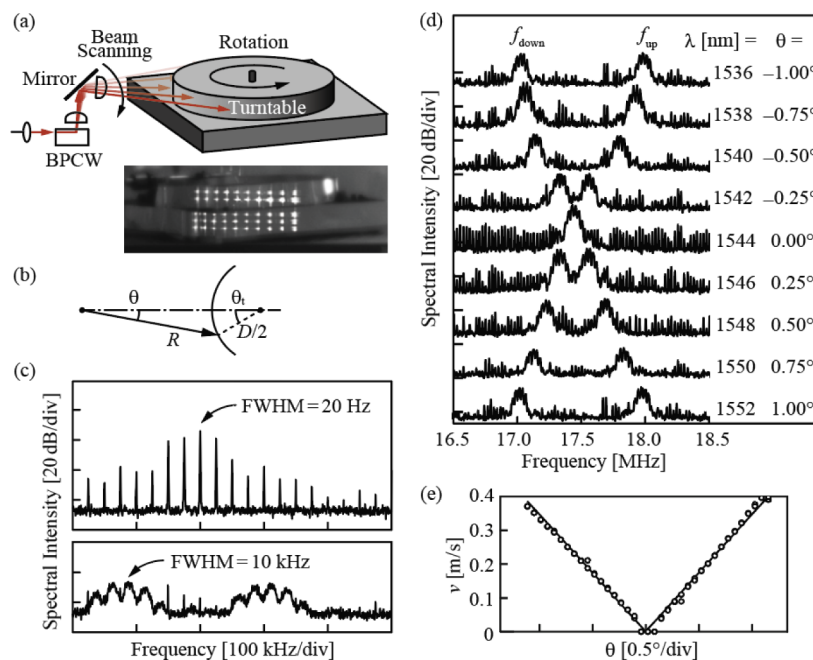

Fig. 2. Measurement of range and velocity of turntable. (a) Schematic of measurement setup and InGaAs camera image of the collimated beam shining on the turntable sidewalls. (b) Parameters of the beam (arrow) and turntable (circular arc). (c) Measured beat spectra at $\theta = -0.25°$. Upper and lower panels show those without and with the rotation of turntable, respectively. (d) Measured spectra with the rotation for different θ changed by the wavelength λ. (e) Comparison between measured velocity (open circle) and theoretical value (solid line).

Further, the turntable was rotated at 45 rpm (tangential velocity $v_t = 0.78$ m/s), and the wavelength was swept for linear beam scanning. At $\lambda = 1554$ nm, the beam shone on the center of the turntable at normal incidence ($\theta = 0°$). At this wavelength, the Doppler shift did not occur due to the absence of velocity components in the direction of light travel. At other wavelengths, the beam was shone on a position other than the center of the turntable, and the Doppler shift clearly appeared, exhibiting the split of the beat frequency into f_{up} and f_{down}. The spectral FWHM expanded to ~10 kHz, and the peak intensity decreased by 30 dB due to jitter, which might be caused by slight eccentricity of the turntable. Figure 2(e) shows the velocity v on the optical axis; the circular plots were measured from the spectral split and the solid line was calculated from

the relation $v = v_t \sin(\theta + \theta_t)$, where $\theta_t = \sin^{-1}[(D/2R)\sin\theta]$. The θ_t at the edge point was $30°$, and the corresponding v was calculated to be 0.40 m/s. The measure value agreed well with this value. The maximum error estimated from the difference between the circular plots and the solid line was 29 mm/s, which is reasonable, considering the range resolution ΔR and the eccentricity. Figure 3 shows the off-line point cloud image created by calculating the range and velocity from Eqs. (1) and (3), respectively. The simultaneous imaging of range and velocity was confirmed. The step-like profile of the fixed pedestal was caused by the range resolution ΔR.
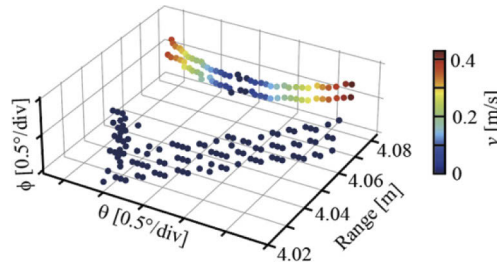

Fig. 3. Point cloud image of range and velocity obtained from mean value and split of the beat spectra.

5. Vibration measurement

For the vibration measurements, we used the same measurement setup shown in Fig. 1, but employed a sawtooth modulation signal with $T = 4$ μs. As shown in Figs. 4(a), speakers (SLP Limited LSE77-20R of 78 mm diameter and 15 kHz cutoff frequency) with reflective sheets (ORALITE AP1000) pasted on the front were used as target objects. The beam spot on this sheet was approximately 10 mm in diameter. Figure 4(b) shows the beat spectrum measured when the speakers were vibrated at various f_v. At this time, the speakers were driven at 8 V_{p-p}, exhibiting maximum sidelobe levels, by a function generator (Agilent 33220A). The noise floor determined by the used setup did not change when the signal generator drove the speakers. As expected from Section 2, sidebands clearly appeared with a frequency spacing of f_v around the beat frequency. At $f_v < 5$ kHz, the spectral intensity distribution is complicated, reflecting higher order sidebands in Eq. (7). In each panel, the vibration amplitude ΔX obtained from Eq. (8) was noted together with the vibration frequency. Figure 4(c) summarizes the relation between ΔX and the applied voltage at $f_v = 5$ kHz. The response was linear up to the rated voltage of 7.5 V_{p-p}. Since the used voltage of 8 V_{p-p} for Fig. 4(b) was higher than this value, the vibration might include harmonic components. We consider that such components were larger for lower f_v and generated extraordinary envelope profiles of the spectra. Even in these situations, we could estimate ΔX as the vibration amplitude of the fundamental frequency from Eq. (8). At $f_v = 3$ kHz and 20 kHz, the intensity ratios in Eq. (8) were 3.5 dB and 35 dB, respectively, which indicated that $\Delta X = 140$ nm and 4.4 nm. When S/N was higher than 40 dB, the detection limit of ΔX was 2.5 nm.

Then, three speakers at different ranges were driven at $f_v = 1.5$ kHz, 2 kHz, and 2.5 kHz, respectively. The beam was scanned in 2D, and the beat spectrum was measured at each resolution point. Figure 5 shows the off-line point cloud image created from the calculated range and measured vibration frequency. The center and right speakers were placed perpendicular to the beam, whereas the left speaker was tilted slightly. Each f_v was represented as a color plot. The measurement error in f_v was simply determined by the spectrum analyzer and was no larger than 10 Hz. Figure 5 also shows the distribution of ΔX for Speaker 1. It is observed that the amplitude was larger at the circular edge of the speaker, to which the retroreflective sheet was attached directly.
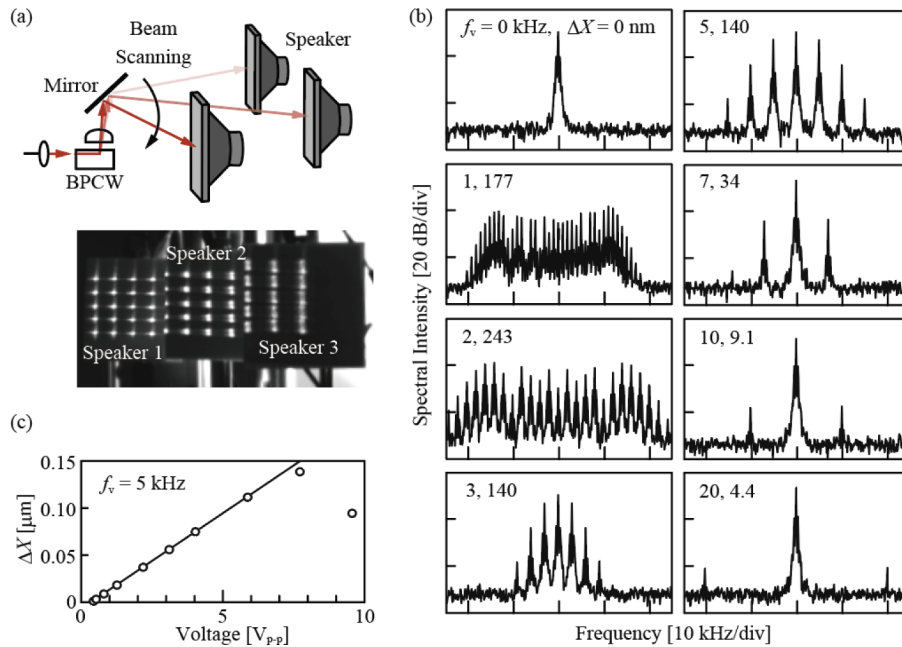
Fig. 4. Measurement of range and vibration distribution. (a) Schematic of the measurement setup and an InGaAs camera image of the collimated beam shining on three speakers. (b) Beat spectrum with sidelobes at different f_v. Estimated ΔX from the sidelobe intensity is also shown. (c) Relation between ΔX and the applied voltage at $f_v = 5$ kHz.
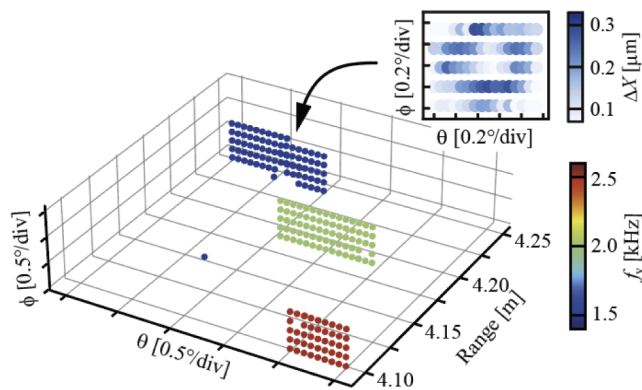

Fig. 5. Point cloud image of range and vibration frequency, which were estimated from the beat spectrum. Upper panel shows the amplitude distribution on Speaker 1 obtained from the sidelobe intensity.

6. Conclusion

We demonstrated the simultaneous measurement of distance, velocity, and vibration in a FMCW LiDAR setup, including a Si photonic crystal beam scanner. In this experiment, the range resolution and velocity resolution were estimated to be 15 mm and 19 mm/s, respectively. The maximum measurement error of the velocity was 29 mm/s, and the detection limit of the vibration amplitude was 2.4 nm. The range resolution could be improved by increasing the frequency bandwidth B. However, the external modulation frequency used was already as high as 10 GHz, and a wider bandwidth becomes a constraint on the system. For this purpose, direct modulation of the laser will be more effective, although it needs some compensation for the nonlinearity. The velocity error might be caused by the eccentricity of the turntable, and the theoretical limit of 19 mm/s will be obtainable for a more accurate target. The resolution can be improved by increasing the period T. The detection limit of the vibration amplitude is determined by the S/N of the beat signal. In this experiment, a retroreflective sheet improved S/N. Without this sheet, the S/N drops by more than 20 dB, and the detection limit is degraded comparably. To ensure similar S/N for arbitrary targets, it will be effective to reduce the fiber coupling loss, improve the upward emission from the BPCW by optimizing its structure, and increase the aperture of the collimator lens.

In this experiment, external components were used except for the beam scanner, but using Si photonics technology, on-chip integration is possible, except for the laser and EDFA. In the future, it is expected that a multimodal FMCW LiDAR with SLDV functionality will be realized on a fingertip-sized chip.

Disclosures. The authors declare no conflicts of interest.

Data availability. Data underlying the results presented in this paper are not publicly available at this time but may be obtained from the authors upon reasonable request.

References

1. B. Shwarz, "Mapping the world in 3D," Nat. Photonics **4**(7), 429–430 (2010).
2. J. Sun, E. Timurdogan, A. Yaacobi, E. S. Hosseini, and M. R. Watts, "Large-scale nanophotonic phased array," Nature **493**(7431), 195–199 (2013).
3. T. Komljenovic, R. Helkey, L. Coldren, and J. E. Bowers, "Sparse aperiodic arrays for optical beam forming and LIDAR," Opt. Express **25**(3), 2511–2528 (2017).
4. D. N. Hutchison, J. Sun, J. K. Doylend, R. Kumar, J. Heck, W. Kim, C. T. Phare, A. Feshali, and H. Rong, "High-resolution aliasing-free optical beam steering," Optica **3**(8), 887–890 (2016).
5. S. W. Chung, H. Abediasl, and H. Hashemi, "A monolithically integrated large-scale optical phased array in silicon-on-insulator CMOS," IEEE J. Solid-State Circuits **53**(1), 275–296 (2018).
6. C. V. Poulton, M. J. Byrd, P. Russo, E. Timurdogan, M. Khandaker, D. Vermeulen, and M. R. Watts, "Long-range LiDAR and free-space data communication with high-performance optical phased arrays," IEEE J. Sel. Top. Quantum Electron. **25**(5), 1–8 (2019).
7. S. A. Miller, Y.-C. Chang, C. T. Phare, M. C. Shin, M. Zadka, S. P. Roberts, B. Stern, X. Ji, A. Mohanty, O. A. J. Gordillo, U. D. Dave, and M. Lipson, "Large-scale optical phased array using a low-power multi-pass silicon photonic platform," Optica **7**(1), 3–6 (2020).
8. W. Bogaerts, M. Dahlem, S. Dwivedi, R. Jansen, and X. Rottenberg, "Dispersive optical phased array circuit for high-resolution pixelated 2D far-field scanning controlled by single wavelength variable," Proc. SPIE **11284**, 69 (2020).
9. D. Inoue, T. Ichikawa, A. Kawasaki, and T. Yamashita, "Demonstration of a new optical scanner using silicon photonics integrated circuit," Opt. Express **27**(3), 2499–2508 (2019).
10. Y.-C. Chang, M. C. Shin, C. T. Phare, S. A. Miller, E. Shim, and M. Lipson, "2D beam steerer based on metalens on silicon photonics," Opt. Express **29**(2), 854–864 (2021).
11. C. Rogers, A. Y. Piggott, D. J. Thomson, R. F. Wiser, I. E. Opris, S. A. Fortune, A. J. Compston, A. Gondarenko, F. Meng, X. Chen, G. T. Reed, and R. Nicolaescu, "A universal 3D imaging sensor on a silicon photonics platform," Nature **590**(7845), 256–261 (2021).
12. H. Ito, Y. Kusunoki, J. Maeda, D. Akiyama, N. Kodama, H. Abe, R. Tetsuya, and T. Baba, "Wide beam steering by slow-light waveguide grating and prism lens," Optica **7**(1), 47–52 (2020).

13. T. Tamanuki, H. Ito, and T. Baba, "Thermo-optic beam scanner employing silicon photonic crystal slow-light waveguides," J. Lightwave Technol. **39**(4), 904–911 (2021).
14. J. Riemensberger, A. Lukashchuk, M. Karpov, W. Weng, E. Lucas, J. Liu, and T. J. Kippenberg, "Massively parallel coherent laser ranging using soliton microcombs," Nature **581**(7807), 164–170 (2020).
15. L. E. Drain, *The laser doppler technique* (Willey, 1980).
16. Y. Li, S. Verstuyft, G. Yurtsever, S. Keyvaninia, G. Roelkens, D. V. Thourhout, and R. Baets, "Heterodyne laser Doppler vibrometers integrated on silicon-on-insulator based on serrodyne thermo-optic frequency shifters," Appl. Opt. **52**(10), 2145–2152 (2013).
17. Y. Li, J. Zhu, M. Duperron, P. O'Brien, R. Schüler, S. Aasmul, M. Melis, M. Kersemans, and R. Baets, "Six-beam homodyne laser Doppler vibrometry based on silicon photonics technology," Opt. Express **26**(3), 3638–3645 (2018).
18. H. H. Nassif, M. Gindy, and J. Davis, "Comparison of laser Doppler vibrometer with contact sensors for monitoring bridge deflection and vibration," NDT & E International **38**(3), 213–218 (2005).
19. H. Tabatabai, D. E. Oliver, J. W. Rohrbaugh, and C. Papadopoulos, "Novel applications of laser Doppler vibration measurements to medical imaging," Sens Imaging **14**(1-2), 13–28 (2013).
20. S. Kakuma, "Frequency-modulated continuous-wave laser radar using dual vertical-cavity surface-emitting laser diodes for real-time measurements of distance and radial velocity," Opt. Rev. **24**(1), 39–46 (2017).
21. Y. Xiong, Z. Peng, G. Xing, W. Zhang, and G. Meng, "Accurate and robust displacement measurement for FMCW radar vibration monitoring," IEEE Sens. J. **18**(3), 1131–1139 (2018).
22. A. Dandridge, A. Tveten, and T. Giallorenzi, "Homodyne demodulation scheme for fiber optic sensors using phase generated carrier," IEEE J. Quantum Electron. **18**(10), 1647–1653 (1982).
23. W. Zhang, W. Gao, L. Huang, D. Mao, B. Jiang, F. Gao, D. Yang, G. Zhang, J. Xu, and J. Zhao, "Optical heterodyne micro-vibration measurement based on all-fiber acousto-optic frequency shifter," Opt. Express **23**(13), 17576–17583 (2015).
24. H. Ito, T. Tatebe, H. Abe, and T. Baba, "Wavelength-division multiplexing Si photonic crystal beam steering device for high throughput parallel sensing," Opt. Express **26**(20), 26145–26155 (2018).